MSDE



PAPER View Article Online



Cite this: DOI: 10.1039/d2me00153e

Tuning a coiled-coil hydrogel via computational design of supramolecular fiber assembly†

Dustin Britton,^a Michael Meleties,^a Chengliang Liu,^a Sihan Jia,^a Farbod Mahmoudinobar, ^{Dab} P. Douglas Renfrew,^b Richard Bonneau^{bcd} and Jin Kim Montclare ^{D*aefg}

The previously reported Q is a thermoresponsive coiled-coil protein capable of higher-order supramolecular assembly into fibers and hydrogels with upper critical solution temperature (UCST) behavior. Here, we introduce a new coiled-coil protein that is redesigned to disfavor lateral growth of its fibers and thus achieve a higher crosslinking density within the formed hydrogel. We also introduce a favorable hydrophobic mutation to the pore of the coiled-coil domain for increased thermostability of the protein. We note that an increase in storage modulus of the hydrogel and crosslinking density is coupled with a decrease in fiber diameter. We further fully characterize our α -helical coiled-coil (Q2) hydrogel for its structure, nano-assembly, and rheology relative to our previous single domain protein, Q, over the time of its gelation demonstrating the nature of our hydrogel self-assembly system. In this vein, we also characterize the ability of Q2 to encapsulate the small hydrophobic small molecule, curcumin, and its impact on the mechanical properties of Q2. The design parameters here not only show the importance of electrostatic potential in self-assembly but also provide a step towards predictable design of electrostatic protein interactions.

Received 22nd July 2022, Accepted 20th October 2022

DOI: 10.1039/d2me00153e

rsc.li/molecular-engineering

Design, System, Application

We have recently designed the drug encapsulating protein, Q, by domain swapping the cartilage oligomeric matrix protein coiled-coil domain, (COMPcc), resulting in positively and negatively charged patches that allows for the protein to undergo hierarchical self-assembly into mesofibers and upper critical solution temperature (UCST) hydrogels. We have also recently highlighted some of the important conditions and parameters that appear to dictate the gelation of Q, notably isoelectric point, electrostatic potential energy, and thermostability. We have used these parameters to engineer a sequel protein, Q2, to undergo faster gelation and increased mechanical integrity by engineering its supramolecular assembly to make thinner and more densely crosslinked fibers. We find that the protein assembly exhibits a large increase in ordered structure while creating thinner fibers. Rheological techniques demonstrate that Q2 is more densely crosslinked, undergoes a nearly 3-fold faster critical time to gelation, and possesses an increased UCST. Where previous coiled-coil fiber designs have utilized charged patches to create physically crosslinked hydrogels, Q2 demonstrates targeted tunability using computational and quantifiable metrics of which we connect to its time-course gelation. The ability to tune hydrogels to different gelation kinetics and material strengths is of growing importance to a diverse field of biomedical applications that require tuned hydrogels ranging from tissue-engineering scaffolds to *in situ* hydrogels for drug delivery.

Introduction

Self-assembling protein-based hydrogels have become increasingly appealing materials for biomedical applications.¹⁻⁴ Higher-order assembly of these proteins commonly results in physical crosslinking in the form of junctions and arbitrary entanglements, resulting in their subsequent gelation.^{5,6} Protein-based hydrogels can be predominantly bifurcated into hydrogels that possess α -helical and β -sheet interactions.⁷ The nature of the protein-protein interactions dictates the impact of hydrophobicity, charge, and various external stimuli on the resulting gelation properties and overall hierarchical assembly as well as their biomedical utility.^{3,7}

^a Department of Chemical and Biomolecular Engineering, New York University Tandon School of Engineering, Brooklyn, New York, 11201, USA. E-mail: montclare@nyu.edu

^b Center for Computational Biology, Flatiron Institute, Simons Foundation, New York, New York, 10010, USA

^c Center for Genomics and Systems Biology, New York University, New York, New York, 10003, USA

^d Courant Institute of Mathematical Sciences, Computer Science Department, New York University, New York, New York, 10009, USA

^e Bernard and Irene Schwartz Center for Biomedical Imaging, Department of Radiology, New York University School of Medicine, New York, New York, 10016,

f Department of Chemistry, New York University, New York, New York, 10012, USA
g Department of Biomaterials, New York University College of Dentistry, New York, 10010, USA

[†] Electronic supplementary information (ESI) available. See DOI: https://doi.org/10.1039/d2me00153e

Paper

Tuning gelation kinetics has been deemed useful for different biomedical applications, with applications often calling for gelation on a specific timescale. For example, slow-gelling systems have been desired for tissue engineering due to their cell compatibility and matrix homogeneity.8 In contrast, systems that gel in <1 h have been viewed as preferable for injectables that call for in situ gelation for drug delivery. 9,10 Several strategies have been employed to tune systems towards faster or slower gelation kinetics such as combining slow- and fast-reacting functional groups,11 modifying crosslinker structure, 12 optimizing of interacting hydrophobic residues,¹³ and screening of the surrounding chemical environment.^{14,15} To undergo gelation through physical crosslinking, the supramolecular assembly must reach a sufficient volume fraction in solution such that interactions between assemblies create networks capable of water retention.16 Particularly, control over the geometry of the supramolecular assembly has been reported to dictate the crosslinking density, viscoelasticity, and kinetics of the hydrogel network.16,17 An important property inherent to these supramolecularly assembling proteins in clinical use is their responsiveness to various physiological conditions such as temperature, pH, and ionic strength.2

Previously, our group has studied the self-assembly and subsequent protofibril assembly of coiled-coil domains, focusing on the coiled-coil domain of collagen oligomeric matrix protein coil (COMPcc), 18,19 which has been used to form various biomaterials and is capable of drug delivery and diagnostics. 20-25 Recently, we have synthesized the coiled-coil hydrogel, Q, by domain swapping its N- and C-terminus around the Q54 residue of COMPcc.26 The resulting Q possesses an electrostatic redistribution of surface charge such that the N-terminus is positively charged and the C-terminus is negatively charged²⁶ leading to the protein undergoing electrostatically driven supramolecular assembly into a hydrogel at concentrations greater than 1 mM and at temperatures below its upper critical solution temperature (UCST) of 16.2 °C, while maintaining its ability to encapsulate and release small hydrophobic molecules.²⁷ We have shown Q to be stimuli-responsive towards changes in pH and ionic strength, allowing its phase transition, including its transition temperature and the gelation kinetics, to be tuned through alteration of the surrounding chemical environment. 14,15

The fiber growth of Q occurs predominantly through electrostatic coupling and the end-to-end alignment of coiled-coils (longitudinally). Less present, Q fiber diameters measure in tens of nanometer range signaling the presence of some side-to-side stacking of coiled-coils (laterally). To control the crosslinking density of our coiled-coil systems, we redesigned Q with the intent to tune its fiber geometry such that supramolecular assembly is decreased (as measured by lateral growth). By manipulating the electrostatic distribution of the surface, we hypothesize that the thinner protofibrils will possess increased solvent-exposed surface area available interaction and thus create increased

crosslinking of the fibers. We show here a time-course structural and rheological characterization of our redesigned hydrogel (Q2), which has been rationally designed for reduced lateral growth. To further explore the drug encapsulation potential of Q2, we assess the relative ability for Q2 to bind the candidate hydrophobic small molecule, curcumin (CCM) and its relative impact on Q2 material properties.

Materials and methods

Materials

Chemically competent M15MA E. coli cells were gifted from David Tirrell at California Institute of Technology. Bactotryptone, sodium chloride (NaCl), yeast extract, tryptic soy agar, ampicillin sodium salt, sodium phosphate dibasic anhydrous (Na₂HPO₄), sodium hydroxide (NaOH), dextrose monohydrate (D-glucose), magnesium sulfate (MgSO₄), calcium chloride (CaCl2), manganese chloride tetrahydrate (MnCl₂·4H₂O), cobaltous chloride hexahydrate (CoCl₂·6H₂O), β -D-1-thiogalactopyranoside isopropyl (IPTG), bicinchoninic acid (BCA) assay kit, Pierce snakeskin dialysis tubing 3.5 K molecular weight cutoff (MWCO), sodium dodecyl sulfate (SDS), Nunc ninety-six well plates, Molecular Probes FluoSpheres (1.0 µm) and BD Clay Adams glass microscopy slides were acquired from Thermo Fisher Scientific. The twenty naturally occurring amino acids, dimethylsulfoxide (DMSO), 3,3',5,5'-tetramethylbenzidine (TMB), nickel(III) chloride hexahydrate (NiCl₂·6H₂O), sodium molybdate dihydrate (Na2MoO4·2H2O), iron(III) chloride (FeCl₃), iron(II) chloride tetrahydrate (FeCl₂·4H₂O), thiamine hydrochloride (vitamin B), thioflavin T (ThT), and copper(II) sulfate pentahydrate (CuSO₄·5H₂O) were purchased from Sigma Aldrich. Hydrochloric acid (HCl), Coomassie® Brilliant Blue G-250 were purchased from VWR. HiTrap FF 5 mL columns for protein purification were purchased from Cytiva Life Sciences. Macrosep and Microsep Advance Centrifugal Devices 3 K MWCO and 0.2 µm syringe filters were purchased from PALL. Acrylamide/bis solution (30%) 29:1, Mini Trans-Blot filter paper, Trans-Blot Transfer Medium (nitrocellulose membrane), and natural polypeptide sodium dodecyl sulfatepolyacrylamide gel electrophoresis (SDS-PAGE) standard were purchased from Bio-Rad. Copper(II) chloride anhydrous (CuCl₂), sodium selenite (Na₂SeO₃), and imidazole were purchased from Acros Organics. Formvar/carbon-coated copper grids (FCF400-Cu) and 1% uranyl acetate for transmission electron microscopy were purchased from Electron Microscopy Sciences. Borosilicate glass capillaries $(0.2 \text{ mm} \times 2 \text{ mm} \times 75 \text{ mm})$ were purchased from VitroCom. Fast-curing two-component epoxy was acquired from JB Weld.

Computational modeling and design of Q2

To assess the iterative effect of mutations on the stability of a Q variant, ROSETTA suite of macromolecular modeling tools (version 3.5) was used. ROSETTA Relax protocol28 was used

MSDE Paper

on protein sequences using the symmetry of COMPcc (PDB: 3V2P) with the all-atom energy score function.²⁹ To assess the isoelectric point (pI), PDB2PQR software (version 3.1.0) was used to set up titration states at room temperature with the amber³⁰ forcefield and propka³¹ pH calculation method. Electrostatic maps and electrostatic potential energies were calculated using Adaptive Poisson-Boltzmann Solver (APBS) (version 3.0.0) from subsequent PDB2PQR input files. In calculation of Rosetta score and electrostatic potential energy, the conserved His tag is negated due to Rosetta's inability define a consistent minimum energy state.

Expression and purification

Q2 and Q protein were each expressed as described previously.²⁷ Briefly, pQE30/Q2 plasmid was cloned and purchased from Integrated DNA Technologies. Q and Q2 were expressed in methionine-auxotrophic M15MA E. coli cells in supplemented M9 minimal media. Expression of each respective protein was induced through the addition of 200 $\mu g \text{ mL}^{-1}$ IPTG when the optical density at 600 nm (OD₆₀₀) reached ~0.8. Following incubation at 37 °C and 350 rpm for 3 hours, cells were harvested by centrifugation at $5000 \times g$ at 4 °C for 30 minutes in an Avanti J-25 centrifuge (Beckman Coulter) and stored at -20 °C until purification. 12% SDS-PAGE was used to confirm expression of the respective proteins. Q2 and Q were purified using affinity chromatography on a cobalt-charged HiTrap IMAC FF 5 mL column with buffer A (50 mM Tris-HCl, 500 mM NaCl, pH 8.0). Protein was eluted using a gradient of buffer B (50 mM Tris-HCl, 500 mM NaCl, 500 mM imidazole, pH 8.0) possessing an imidazole concentration range from 10-500 mM. Pure fractions were dialyzed in six consecutive 5 L volumes of buffer A and concentrated to 2 mM using 3 kDa Macrosep centrifugal filters (Pall). Protein purity was confirmed by 12% SDS-PAGE and concentration determined by BCA assay.

Tube inversion test

Immediately after concentration to 2 mM, the protein was incubated at 4 °C over the course of two weeks after aliquoting 150 μL into a 2 mL Eppendorf tube. The samples were visually assessed for gelation by inverting the tubes at 12-hour time intervals thereafter, with gelled samples not flowing upon inversion.

Microrheology

Protein was concentrated to 2 mM, as measured by BCA assay, and immediately aliquoted 27.7 µL into a 200 µL PCR tube. 1% v/v (or 0.3 µL) of 1 µm diameter red polystyrene fluorometric beads (FluoSpheres) were then added to the sample. A glass capillary tube was then loaded with sample by capillary action and sealed to prevent evaporation while being affixed to a microscopy slide using two-component fast-curing epoxy (JB Weld).15 Samples were then imaged at 0 h as a starting measurement and then every 12 h using an inverted fluorescent microscope (ZEISS Microscopy) at 40× magnification with 2 × 2 binning. Between imaging, slides were incubated on a rotisserie at 8 rpm to prevent sedimentation of the fluorometric beads. Each image series was recorded for a total of 300 frames with a lag time (τ) of 0.037 s between each frame. Relaxation exponents i.e., the logarithmic slopes of particle mean-squared displacements (MSDs) with respect to lag time as determined by multiple particle tracking (MPT) analysis were used to determine when equilibration of the hydrogel was complete measurements were no longer recorded (60 h in this case). Images were stacked and converted to grayscale in MATLAB (Mathworks, R2021a) using code developed in-house, with MPT then being employed using MATLAB code developed and modified by Dufresne, Kilfoil, Blair, and O'Neill as described previously.15

Curcumin binding

Q2 hydrogels were bound to curcumin and encapsulation efficiency was calculated as previously described.27 150 µL samples of 2 mM Q2 were allowed to gel for 96 h prior to the addition of 300 µL of 1 mM curcumin (dissolved in 50 mM Tris, 500 mM NaCl, 5% DMSO, pH = 8.0). The curcumin was allowed to absorb through the top of the hydrogels for a total of 48 h. Supernatant was then removed and assessed for curcumin concentration by comparing to a standard curve of curcumin (dissolved in 50 mM Tris, 500 mM NaCl, 5% DMSO, pH = 8.0) characterized spectrophotometrically via absorbance at 410 nm by a BioTek Synergy H1 microplate reader at room temperature (RT).

Rheology

Mechanical integrity of the Q2 hydrogel was assessed using a stress-controlled rheometer (Discovery Hybrid Rheometer 2, TA Instruments) equipped with a parallel plate geometry. After complete gelation of a 2 mM sample at 4 °C, the sample was loaded onto the 8 mm diameter lower and upper plates with a 0.2 mm geometry gap. Curcumin-bound Q2 samples were measured in duplicate after 48 h of curcumin absorption following removal of supernatant and buffer wash. Strain and frequency settings were informed from previous Q hydrogel studies²⁷ where the storage modulus (G')and loss modulus (G'') were measured over the frequency range 0.1-10 Hz with a 5% oscillation strain.

Circular dichroism spectroscopy

Secondary structure of Q2 was measured using a Jasco J-815 CD spectrometer with a PTC-423S single position Peltier temperature control system. Wavelength scans were performed from 195 to 250 nm at 1 nm step sizes by diluting 2 mM of the protein into water in order to minimize the effects of sodium chloride. Scans were performed of Q2 before and after gelation at 4 °C at 15 and 20 µM respectively. The mean residue ellipticity (MRE) was calculated as described in previous studies.¹⁸

Attenuated total reflectance-Fourier transform infrared spectroscopy

Secondary structure of Q2, CCM-bound Q2, and Q protein were confirmed using attenuated total reflectance-Fourier transform infrared (ATR-FTIR) spectroscopy using a Nicolet 6700 Fourier transform infrared spectrometer equipped with a diamond ATR accessory and a mercury cadmium telluride (MCT)-A detector. Spectra were collected for 5 μ L of 2 mM protein from 4000–400 cm⁻¹ with 0.5 cm⁻¹ increments. Sample spectra were normalized using buffer background and analyzed from 1700–1600 cm⁻¹ corresponding to the amide I region. Peaks were deconvoluted using Gaussian functions in PeakFit software until the goodness of fit reached $r^2 \geq 0.99$. 32,33

Transmission electron microscopy

Transmission electron microscopy (TEM) images were taken with a FEI Talos L120C transmission electron microscope for Q2 and Q and with a FEI Tecnai Spirit for CCM-bound Q2 at 120 kV. The supramolecular assembly of Q2 and Q were monitored over the course of 60 and 144 hours, respectively (in correspondence with tube inversion and microrheology). TEM images were taken of the gel at times consistent with when microrheological measurements were made for Q2 for consistent fibril sizing. TEM images were also taken of Q2 following binding to CCM. Samples were first diluted to 50 μ M and 3 μ L were spotted on Formvar/carbon-coated copper grids followed by a 5 μ L wash with water, and 3 μ L staining with 1% v/v uranyl acetate solution each with incubation times of 1 min. Following imaging, fibrils were sized in ImageJ software (version 1.52q). 34

Statistical analysis

GraphPad Prism (GraphPad software) was employed for statistical analysis using student's t-test. Python sklearn

module was employed for regression analysis of phase diagrams.

Results and discussion

Design

Q2 was previously designed³⁵ to assemble into thinner nanofibers relative to Q by reduced lateral supramolecular assembly (Fig. 1). Briefly, our group has noted that Q shows faster gelation and increased storage modulus at pH near its pI. 14,15 Similarly, end-to-end stacking of protofibrils into nanofibers is conserved in COMPcc18,26,36 despite its lower overall electrostatic potential energy $(U_{\rm E})$. Thus, we hypothesize that a lower overall $U_{\rm E}$ might preferentially reduce the interaction of neighboring coiled-coils without removing the ability for supramolecular assembly into nanofibers. We iteratively assessed rationally chosen mutations to improve protein stability using Rosetta relax and score functions, APBS to calculate $U_{\rm E}$. This was done until we discovered a design with a negatively redistributed surface, lower pI, lower overall $U_{\rm E}$, and improved Rosetta score. A final design (Fig. 1) was chosen, with a Rosetta score of -637 kcal mol⁻¹ and pI 8.2 compared to the Rosetta score of -619 kcal mol-1 and pI 9.7 for the parent Q protein, suggesting increased propensity for protein-protein interactions at neutral pH and a higher stability for Q2. Q2 possessed a lower $U_{\rm E}$ of 1.29×10^5 kJ mol⁻¹ compared to that of Q at 2.19 × 105 kJ mol-1 suggesting reduced potential for protein-protein interaction.

Gelation

To study the relative gelation of Q2 as compared to the previously reported coiled-coil hydrogel, Q, protein was successfully expressed (Fig. S1†), purified (Fig. S2†), and concentrated to 2 mM (1.3% w/v) in Tris buffer (50 mM Tris, 500 mM NaCl) at pH 8.0. Purity of the protein was measured to be >99% by SDS-PAGE (Fig. S3†) and concentration was

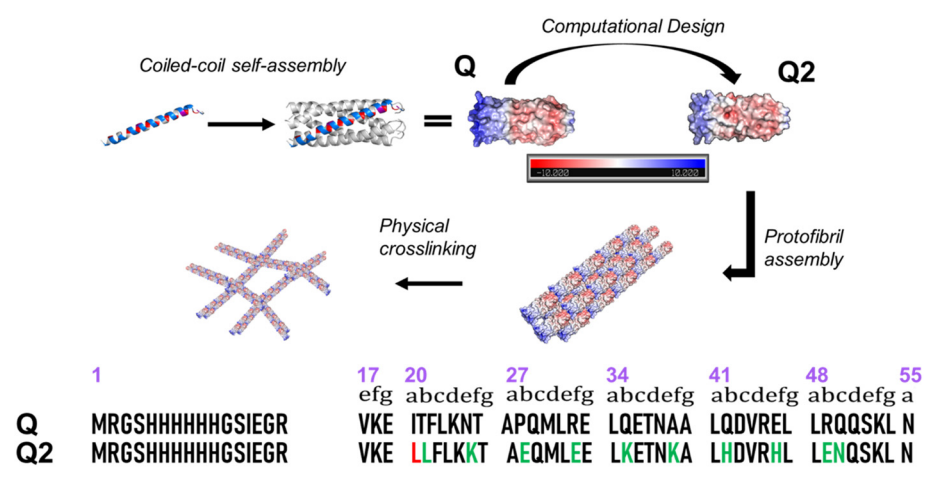


Fig. 1 Path of supramolecular assembly for Q and Q2 hydrogels. Electrostatic potential maps for Q and Q2 show negative (red) and positive (blue) charged patches scaled from -10 kbT/e to 10 kbT/e. Sequences for Q and Q2 with position numbers. Mutations are highlighted for the hydrophobic pore (red) and charged solvent exposed surface (green).

MSDE Paper

measured by **BCA** assay. **Immediately** following concentration, the gelation process of Q2 was studied using the microrheology assay described previously following incubation at 4 °C. 15 Separately, 150 µL samples were aliquoted for tube inversion tests performed after 2 weeks of incubation for visual assessment of gelation over time at 4 °C (Fig. 2a-d) and at concentrations from 1 mM to 3.5 mM with temperatures 5 °C to 25 °C using 0.5 mM and 5 °C step sizes, respectively, to create a matrix-based phase diagram (Fig. 2e). Temperature and concentration ranges were selected based on preliminary tube-inversion testing at high and low ends of the anticipated ranges. Protein concentrated past 3.5 mM was observed to precipitate out of solution at 25 °C, indicating a solubility limit to our phase diagram, as also noted in the UCST phase diagram of the parent protein, Q.²⁷ In contrast, the UCST of Q2 was determined using sklearn linear processing in Python, where a bivariate linear relationship for the extent of gelation was established, assigning all tubes that passed for a gel by tube inversion (shown in red in Fig. 2e) a value of 1 and all tubes that failed to form a gel by tube inversion (shown in black in Fig. 2e) a value of 0. The relationship represented by the heatmap (Fig. S4†) resolved a similar gelation system noted by the thirddegree polynomial fit in Hill et al. that revealed an apparent maximum gelation temperature near the end of the concentrations used.27 Alternatively, we established an interpolated UCST of 22.0 °C at the end of our solubility limit, 3.5 mM; we used our linear relationship to solve for an extent of gelation, η , value of 0.5, representing the transition point of a material that is between a gel and solution. In comparison, the same analysis on the phase boundary points in Hill et al.27 represented a UCST of 17.0 °C, at the end of

the solubility limit for Q, 3.5 mM, resulting in an increase of 5 °C in the UCST (Fig. 2).

From this relationship, coefficients for the dependence of gelation on temperature and concentration can be determined. We use these to compare the UCST dependence on concentration and temperature. In comparison, we note a concentration coefficient of 0.251 mM⁻¹ and 0.247 mM⁻¹ for Q2 and Q, respectively; moreover, there is a temperature coefficient of -0.050 °C⁻¹ and -0.091 °C⁻¹ for Q2 and Q, respectively. This translates to a 2% increase in concentration dependence and 45% decrease in temperature dependence from Q to Q2. Using this independent component analysis, Q2 shows both a stronger enthalpic drive to gelation, which can be attributed to its favorable stability due to sequence optimization (T21L, N25K, P28E, R32E, Q35K, Q42H, E46H, R49E, and Q50N) and introduction of the I20L mutation supported by a higher Rosetta score, and entropic drive to gelation, which we attribute to improved surface charge and a pI closer to the buffer pH (8.0) used in the characterization of Q and Q2. In this regard, the increase in UCST of Q2 compared to that of Q, as well as rheological properties, is most dependent on its concentration.

The solution-to-gel (sol-gel) transition with respect to time was quantified at 2 mM and 4 °C using passive microrheology. MPT analysis was employed to assess the movement of fluorescent tracer beads (FluoSphere), with bead trajectories tracked every 6 hours and their MSDs analyzed using a best-fit sigmoidal analysis15 in MATLAB. Plotting the relaxation exponent with respect to time revealed a plateau, consistent with an equilibrating hydrogel, after 60 hours (Fig. S5†). While the logarithmic slope of the particle

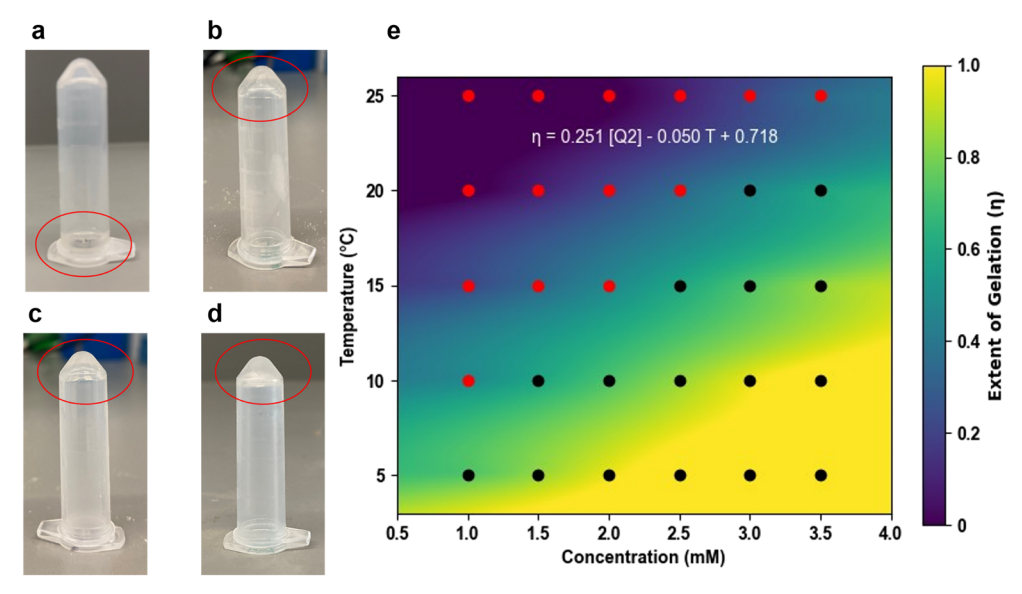


Fig. 2 Tube inversion images of 150 μL aliquots of Q2 at a. 0 h showing a liquid phase fallen to the bottom of the tube. b. 12 h showing the transition between a solution and gel state c. 36 h showing almost complete transition from solution to gel and d. complete transition to gel noted by zero visual movement of the gel at the top of the Eppendorf when inverted. e. Extent of gelation calculated by bivariate linear regression of a concentration-temperature phase diagram constructed from tube inversions showing gel behavior (black dots) and tube inversions showing solution behavior (red dots) after two weeks of incubation at 4 °C.

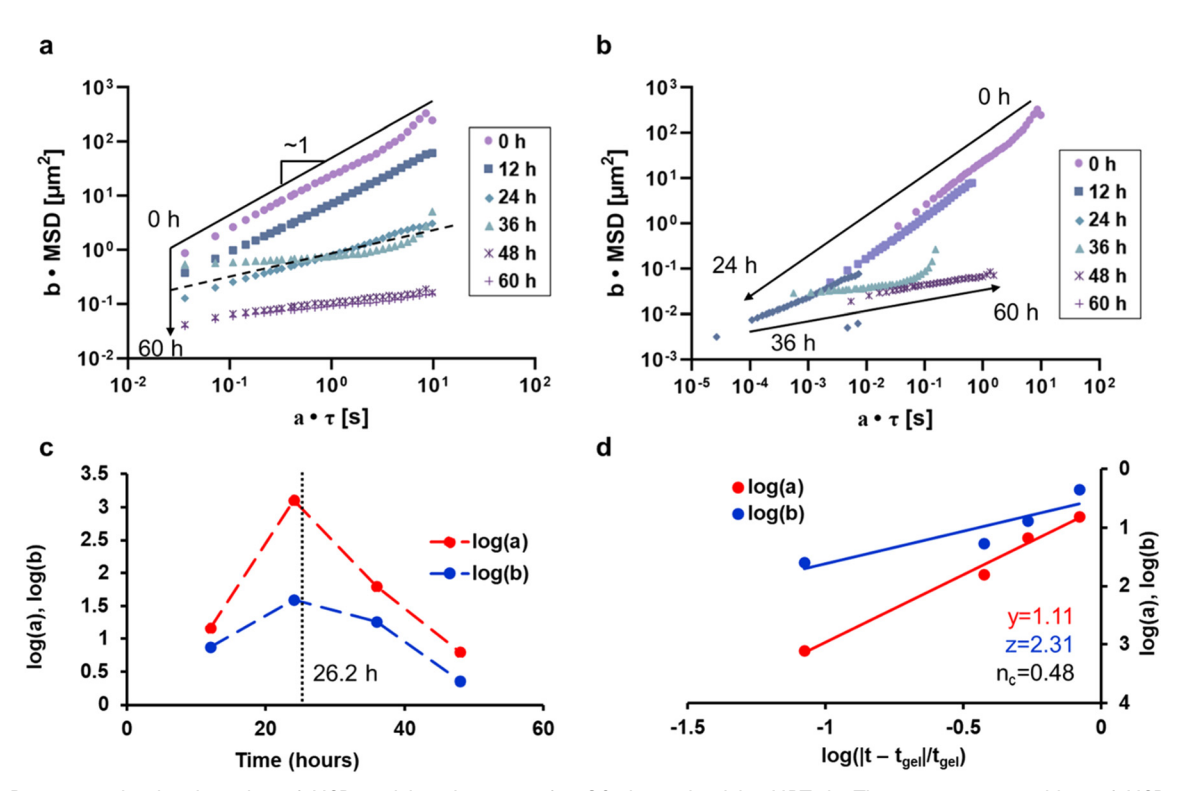


Fig. 3 a. Representative log-log plot of MSD and lag time, tau, for Q2 determined by MPT. b. Time-cure superposition of MSD vs. tau. c. Logarithmic shift factors for the vertical (log(a) in blue) and horizontal (log(b) in red) directions used in the time cure superposition to the determine the t_{gel} . d. Log-log plot of the shift factors and their distance from the t_{gel} determined by the ratio of the logarithmic slopes of the horizontal to vertical shift factor.

mean-square displacements (MSDs) began at 1.00 \pm 0.03 μ m² s⁻¹ (consistent with Brownian motion), a gelation plateau was observed at 0.18 \pm 0.06 μm^2 s⁻¹ suggesting viscoelastic behavior of the final material³⁷ (Fig. 3a). The respective MSD- τ curves for these relaxation exponents were selected as the master solution and master gelation curves, respectively, for time-cure superposition analysis, Q2 exhibited statistically insignificant differences compared to the master curves used for Q^{27} by an unpaired t-test (p-values 0.99 and 0.88, respectively) indicating similar gelation kinetics. Intermediate MSD-7 curves (between 0 h and 60 h) were superimposed onto the master solution or master gelation curve using horizontal and vertical shift factors, a and b, respectively (Fig. 3b). A divergence in the superposition onto the respective master curves was consistently seen between 24 h and 36 h, narrowing the time frame of the sol-gel transition to this window. As done previously, the asymptotic behavior of the shift factors as the critical extent of gelation is approached was used to determine the time to gelation, t_{gel} (Fig. 3c). Dynamic scaling factors, y and z, determined from the slopes of the horizontal and vertical shift factors, respectively, in relationship to the t_{gel} were used to calculate the critical relaxation exponent, n_c , which is characteristic of the degree of crosslinking (Fig. 3d). 38 Q2 possessed a t_{gel} of 26.6 \pm 0.5 h, revealing a large increase in the gelation kinetics compared to the Q hydrogel. A significant increase in crosslinking density of Q2 is suggested by an n_c of 0.48 \pm

0.001 as compared to Q $(n_c = 0.53 \pm 0.03)^{27}$ by an unpaired *t*-test (*p*-value = 0.045).

After gelation, rheological analysis of the storage and loss moduli was performed to assess the macroscopic mechanical integrity of Q2 (Fig. 4, Table S2†). As done previously for Q, a frequency sweep from 0.1 Hz to 10 Hz was performed at an oscillation strain of 5%. 27 Q2 showed a strong improvement in mechanical integrity with a near 6-fold improvement in storage modulus reported at 10 Hz with a G^\prime of 289.6 \pm 86.9 Pa compared to 50.4 Pa for Q. 27 In a physically crosslinked

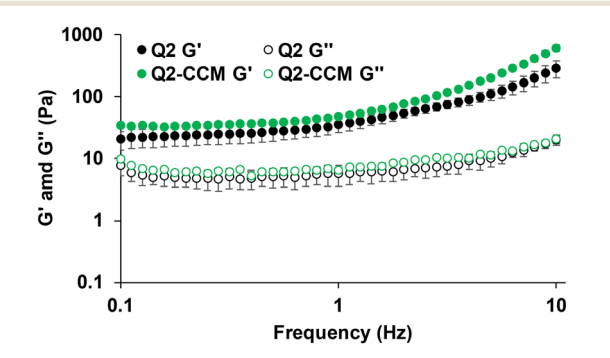


Fig. 4 Rheology of Q2 measured using parallel plate rheometer setup for average storage modulus (G', filled markers) and average loss modulus in (G'', empty markers) of Q2. Error bars represent standard deviation for three independent trials Q2 and two independent trials Q2-CCM.

MSDE

system, a higher G' is associated with a higher degree of crosslinking,³⁸ which is consistent with the lower critical exponent determined through relaxation superposition.

In CCM-bound Q2 samples, the storage modulus exhibited a 2-fold improvement compared to the unbound O2, with a G' of 610.6 \pm 69.4 Pa (Fig. 4, Table S3 \dagger), indicative of an even larger increase in crosslinking and entanglement as compared to the 1.7-fold improvement exhibited by Q when bound to CCM with a G' of 88.0 Pa.²⁷ Interestingly, After 48 h of incubation with CCM at 4 °C, O2 measured an encapsulation efficiency of $80.0 \pm 0.8\%$ as compared to $52.3 \pm$ 0.9% in Q,²⁷ a 1.5-fold improvement as compared to Q. These results agree with our previous work showing that curcumin can stabilize the protein network and improve hydrogel supramolecular assembly.^{27,39} Thus, the increase in encapsulation efficiency can explain the greater relative increase in storage modulus.

Secondary structural changes upon gelation

ATR-FTIR and CD spectroscopy were used to analyze protein secondary structure before and after gelation. In solution, immediately following concentration to 2 mM, Q2 revealed a typical α-helical protein secondary structure noted by CD wavelength scans performed at 4 °C, showing a doubleminima of $-3400 \pm 1000 \text{ deg cm}^2 \text{ dmol}^{-1}$ at 208 nm and $-2600 \pm 600 \text{ deg cm}^2 \text{ dmol}^{-1}$ at 222 nm, indicative of helical conformation (Fig. 5a). The wavelength signature was similar to that of Q.27 Moreover, ATR-FTIR revealed helical conformation for Q2 (Fig. 5bi) similar to Q (Fig. S9a, Table S4†). Following incubation at 4 °C for one week and confirmation of gelation, secondary structure of O2 in the hydrogel state was assessed (Fig. 5aii and bii). Both CD and FTIR spectra reveal a substantial increase in structured content. Notably, the CD spectrum of Q2 post-gelation exhibited a single minimum at 227 nm of -3600 ± 800 which may be characteristic of a linear combination of α -helix and β-sheet conformation. 40,41 Significantly, the Q2 spectra postgelation exhibited a 222/208 ratio of 3.35 \pm 0.37 where helical systems with 222/208 ratios >1 have been used to indicate the likelihood of the α -helix being found within a coiled-coil structure rather than in isolation. 42-44

Deconvolution of FTIR spectra reveals an increase in α -helical conformation (+12.8%) at the expense of β -sheet conformation (-4.5%) and random coil conformation (-3.2%), indicating that the structure become more helical upon gelation (Table S4†), similarly to Q (43%) (Fig. S9b, Table S4†). Finally, upon binding CCM, Q2 secondary structure again shifts towards increased conformation (increasing by 5.4% to 40.4%) (Fig. S10, Table S4†). This shift also occurs in previously reported CCM binding of Q.27 We have also recently shown that Q2 and Q dock CCM similarly by in silico models using Rosetta where

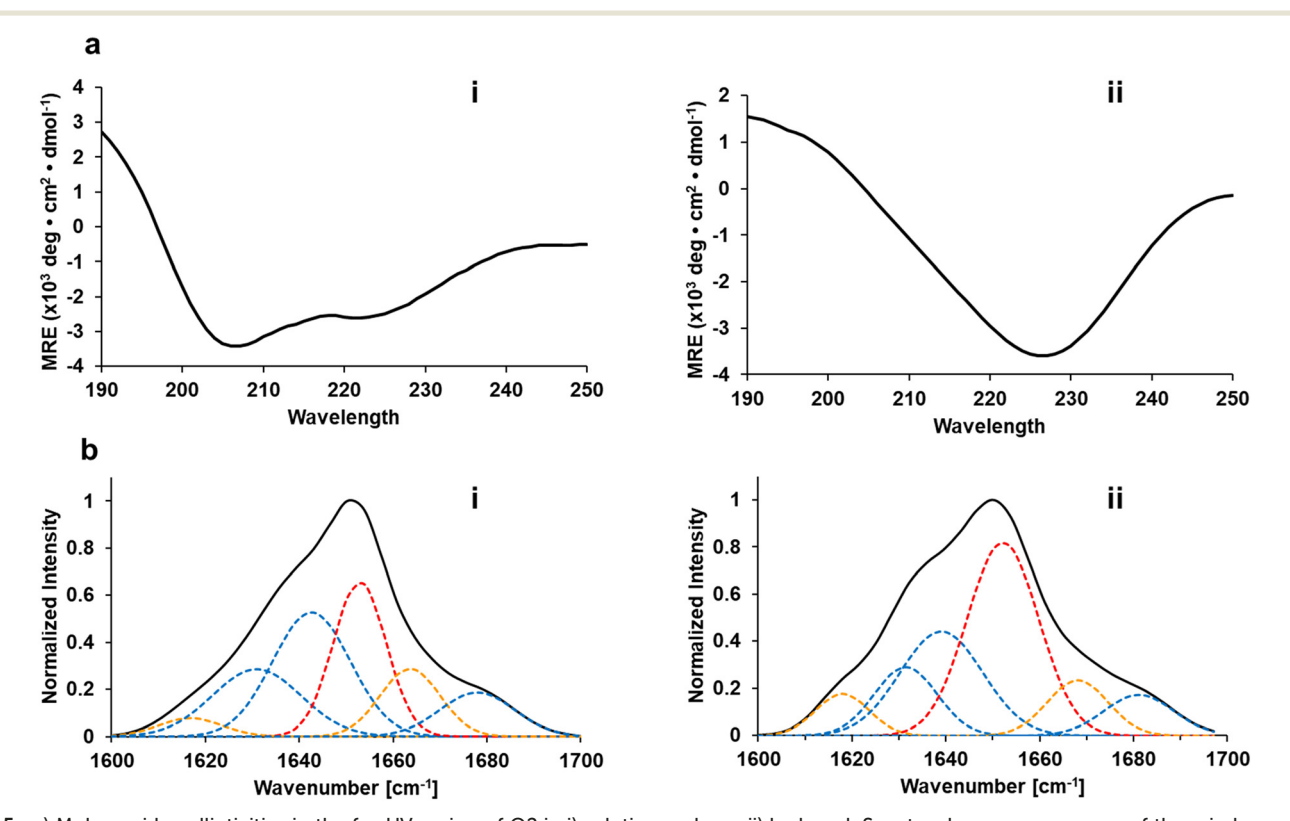


Fig. 5 a) Molar residue ellipticities in the far-UV region of Q2 in i) solution and as a ii) hydrogel. Spectra shown are averages of three independent trials. b) Representative ATR-FTIR spectral analysis of Q2 secondary structure in i) solution state and as a ii) hydrogel. Overall spectra by deconvolution in black and individual peak deconvolutions in dotted red lines (α -helix), blue lines (β -sheet), and orange lines (random coil/turns).

MSDE Paper

Q2 and Q possess interface scores of -46.3 kcal mol⁻¹ and -46.2 kcal mol⁻¹, respectively.³⁵ The similar ATR-FTIR and behavior of CCM-bound Q2 shown here further confirm that CCM exhibits a positive interaction inside the hydrophobic pore of the coiled-coil eliciting an increase in α -helicity and stability.

Nanoscale assembly and hydrogel microstructure

To assess the morphology and structure of the Q2 hydrogel over time, samples were imaged through TEM at 0 h, 12 h, 36 h, and 60 h. Whereas at 0 h, Q2 displayed unorganized protein deposits or aggregates, the formation of nanometerscaled fibrous structures was observed at 12 h. By 36 h, Q2 demonstrated a high degree of physical crosslinking characteristic of a networked hydrogel. At 60 h where equilibrated gelation was observed by microrheology, the hydrogel network became more densely crosslinked, which is consistent with rheological measurements of the hydrogel.

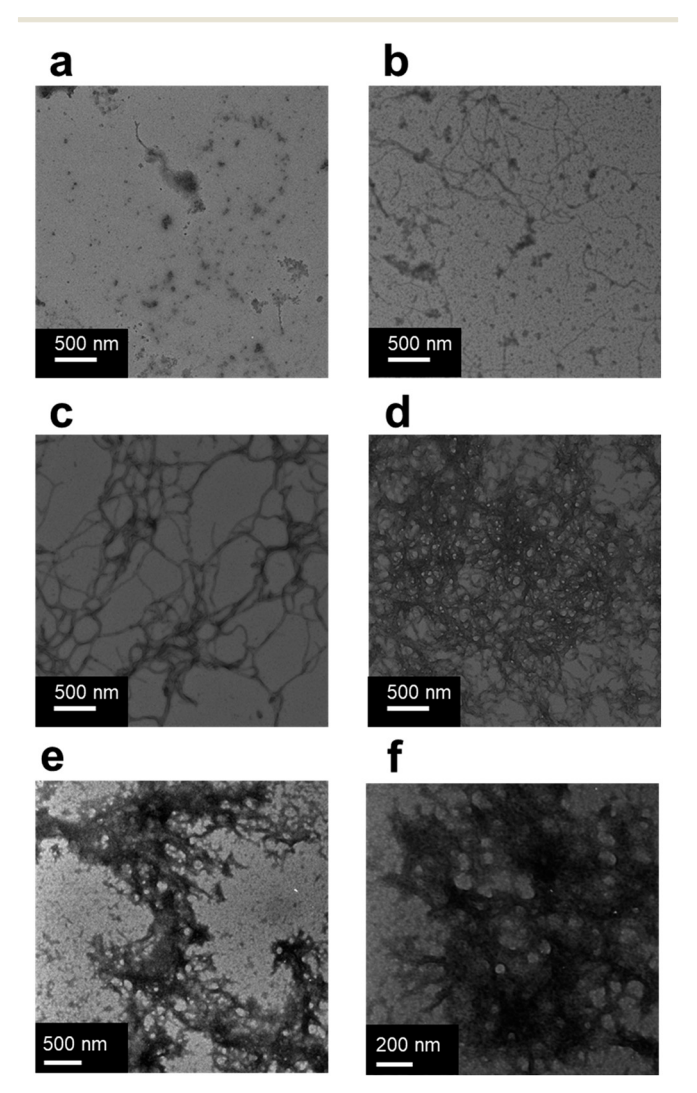


Fig. 6 TEM images at times a) 0 h, b) 12 h, c) 36 h, and d) 60 h and e and f) after CCM binding.

To investigate the effect of lateral assembly, micrograph images of Q2 (Fig. 6a-d) and Q (Fig. S8a-d†) were used to assess the physically crosslinked hydrogel microstructure. In the final hydrogel structures, Q2 displayed interconnected fibril diameters of 28.9 \pm 8.6 nm, which is significantly less than the microstructures resolved by O's hydrogel network with average diameters of 40.5 ± 25.2 nm (p-value = 0.0001) indicating a decrease in the lateral assembly of protofibrils. At this point, only organized fibril networks were visible with noticeable aggregates. Coupled with rheological measurements, protofibril formation of Q2 disfavored lateral assembly while conserving longitudinal assembly, resulting in thinner fibers that yielded more densely crosslinked networks. Finally, CCM-bound Q2 hydrogels display a densified hydrogel network (Fig. 6e and f). The improved mechanical integrity, appearance of increased network density, and improved encapsulation efficiency not only suggests that CCM increases nanofiber interaction of our coiled-coil hydrogel systems (Q and Q2), but that the increased crosslinking inherent of Q2 confers increased interactions with CCM thus imbuing a greater impact on its rheology.

Conclusions

We have engineered a new single domain coiled-coil hydrogel to increase its UCST, mechanical integrity, and gelation kinetics through iterative rational design using protein stability and surface charge to undergo decreased lateral fiber assembly. To fully assess the impact of these changes, we explored a time-course study on structure and gelation properties of Q2 compared to Q. The results demonstrate a higher density of crosslinking as a result of its design. The favorability of these design choices for reduced lateral assembly can potentially be used to tune the gelation properties of physically crosslinked hydrogels supramolecular assemblies. With improved crosslinking density, we also explore the improved encapsulation of CCM by Q2 as compared to Q and its increased impact on its rheological properties. This bottom-up approach may inform design choices to tune hydrogel gelation properties for various biomedical applications and understand the change in morphology and secondary structure over time.

Author contributions

The manuscript was written through contributions of all authors. All authors have given approval to the final version of the manuscript.

Conflicts of interest

The authors declare no competing financial interests.

MSDE Paper

Acknowledgements

This work was supported by NSF-DMREF under Award Number DMR 1728858 and input by the NSF-MRSEC Program under Award Number DMR 1420073. ATR-FTIR experiments were performed at the NYU Chemistry Department Shared Instrument Facility. We would like to thank Professor Weiqiang Chen and Dr. Chao Ma for their assistance providing time and access to their fluorescent microscope for microrheology data collection. We also would like to thank Mike Bucaro and the Advanced Imaging Facility (AIF) at The City University of New York – College of Staten Island for their availability and assistance with transmission electron microscopy instrumentation required for experiments of CCM-bound Q2.

References

- S. Banta, I. R. Wheeldon and M. Blenner, *Annu. Rev. Biomed. Eng.*, 2010, 12, 167–186.
- 2 P. Katyal, F. Mahmoudinobar and J. K. Montclare, *Curr. Opin. Struct. Biol.*, 2020, **63**, 97–105.
- 3 P. Katyal, M. Meleties and J. K. Montclare, ACS Biomater. Sci. Eng., 2019, 5, 4132–4147.
- 4 J. Kopeček and J. Yang, Angew. Chem., Int. Ed., 2012, 51, 7396-7417.
- 5 R. S. Tu and V. Breedveld, *Phys. Rev. E: Stat., Nonlinear, Soft Matter Phys.*, 2005, 72, 041914.
- 6 L. J. Dooling, M. E. Buck, W.-B. Zhang and D. A. Tirrell, Adv. Mater., 2016, 28, 4651–4657.
- 7 J. Chen and X. Zou, *Bioact. Mater.*, 2019, 4, 120–131.
- 8 E. A. Growney Kalaf, R. Flores, J. G. Bledsoe and S. A. Sell, *Mater. Sci. Eng.*, *C*, 2016, **63**, 198–210.
- 9 S. R. Van Tomme, G. Storm and W. E. Hennink, *Int. J. Pharm.*, 2008, 355, 1–18.
- 10 P. Katyal, A. Hettinghouse, M. Meleties, S. Hasan, C. Chen, M. Cui, G. Sun, R. Menon, B. Lin, R. Regatte, J. K. Montclare and C.-J. Liu, *Biomaterials*, 2022, 281, 121370.
- 11 M. Patenaude, S. Campbell, D. Kinio and T. Hoare, *Biomacromolecules*, 2014, **15**, 781–790.
- 12 E. Jain, L. Hill, E. Canning, S. A. Sell and S. P. Zustiak, J. Mater. Chem. B, 2017, 5, 2679–2691.
- 13 C. Chen, Y. Gu, L. Deng, S. Han, X. Sun, Y. Chen, J. R. Lu and H. Xu, *ACS Appl. Mater. Interfaces*, 2014, **6**, 14360–14368.
- 14 M. Meleties, P. Katyal, B. Lin, D. Britton and J. K. Montclare, Soft Matter, 2021, 17, 6470–6476.
- 15 M. Meleties, D. Britton, P. Katyal, B. Lin, R. L. Martineau, M. K. Gupta and J. K. Montclare, *Macromolecules*, 2022, 55, 1239–1247.
- 16 M. L. Oyen, Int. Mater. Rev., 2014, 59, 44-59.
- 17 V. K. Lai, C. R. Frey, A. M. Kerandi, S. P. Lake, R. T. Tranquillo and V. H. Barocas, *Acta Biomater.*, 2012, 8, 4031–4042.
- 18 S. K. Gunasekar, M. Asnani, C. Limbad, J. S. Haghpanah, W. Hom, H. Barra, S. Nanda, M. Lu and J. K. Montclare, *Biochemistry*, 2009, 48, 8559–8567.

19 L. Yin, A. S. Agustinus, C. Yuvienco, T. Miniashima, N. S. Schnabel, T. Kirsch and J. K. Montclare, *Biomacromolecules*, 2018, 19, 1614–1624.

- 20 L. K. Hill, J. A. Frezzo, P. Katyal, D. M. Hoang, Z. B. Youss, C. Xu, X. Xie, E. Delgado-Fukushima, Y. Z. Wadghiri and J. K. Montclare, ACS Nano, 2019, 13, 2969–2985.
- 21 A. J. Olsen, J. S. Haghpanah, P. Katyal, N. S. Schnabel, M. Dai, N. Singh, R. S. Tu and J. K. Montclare, *Biomacromolecules*, 2018, **19**, 1552–1561.
- 22 M. Dai, J. A. Frezzo, E. Sharma, R. Chen, N. Singh, C. Yuvienco, E. Caglar, S. Xiao, A. Saxena and J. K. Montclare, I. Nanomed. Nanotechnol., 2016, 7, 356.
- 23 M. Dai, J. Haghpanah, N. Singh, E. W. Roth, A. Liang, R. S. Tu and J. K. Montclare, *Biomacromolecules*, 2011, 12, 4240–4246.
- 24 J. S. Haghpanah, C. Yuvienco, E. W. Roth, A. Liang, R. S. Tu and J. K. Montclare, *Mol. BioSyst.*, 2010, 6, 1662–1667.
- 25 J. S. Haghpanah, C. Yuvienco, D. E. Civay, H. Barra, P. J. Baker, S. Khapli, N. Voloshchuk, S. K. Gunasekar, M. Muthukumar and J. K. Montclare, *ChemBioChem*, 2009, 10, 2733–2735.
- 26 J. Hume, J. Sun, R. Jacquet, P. D. Renfrew, J. A. Martin, R. Bonneau, M. L. Gilchrist and J. K. Montclare, *Biomacromolecules*, 2014, 15, 3503–3510.
- 27 L. K. Hill, M. Meleties, X. Xie, E. Delgado-Fukushima, T. Jihad, C. F. Liu, S. O'Neill, R. S. Tu, P. D. Renfrew, R. Bonneau, Y. Z. Wadghiri and J. K. Montclare, *Biomacromolecules*, 2019, 20, 3340–3351.
- 28 L. G. Nivón, R. Moretti and D. Baker, PLoS One, 2013, 8, e59004.
- 29 R. F. Alford, A. Leaver-Fay, J. R. Jeliazkov, M. J. O'Meara, F. P. DiMaio, H. Park, M. V. Shapovalov, P. D. Renfrew, V. K. Mulligan, K. Kappel, J. W. Labonte, M. S. Pacella, R. Bonneau, P. Bradley, R. L. Dunbrack, Jr., R. Das, D. Baker, B. Kuhlman, T. Kortemme and J. J. Gray, J. Chem. Theory Comput., 2017, 13, 3031–3048.
- 30 W. D. Cornell, P. Cieplak, C. I. Bayly, I. R. Gould, K. M. Merz, D. M. Ferguson, D. C. Spellmeyer, T. Fox, J. W. Caldwell and P. A. Kollman, J. Am. Chem. Soc., 1995, 117, 5179–5197.
- 31 D. C. Bas, D. M. Rogers and J. H. Jensen, *Proteins: Struct.*, *Funct.*, *Bioinf.*, 2008, 73, 765–783.
- 32 P. Wang, W. Bohr, M. Otto, K. M. Danzer and B. Mizaikoff, *Anal. Bioanal. Chem.*, 2015, **407**, 4015–4021.
- 33 X. Hu, D. Kaplan and P. Cebe, *Macromolecules*, 2006, **39**, 6161–6170.
- 34 C. A. Schneider, W. S. Rasband and K. W. Eliceiri, *Nat. Methods*, 2012, 9, 671–675.
- 35 D. Britton, J. Monkovic, S. Jia, C. Liu, F. Mahmoudinobar, M. Meleties, P. D. Renfrew, R. Bonneau and J. K. Montclare, *Biomacromolecules*, 2022, DOI: 10.1021/acs.biomac.2c01031.
- 36 H. T. More, K. S. Zhang, N. Srivastiva, J. A. Frezzo and J. K. Montclare, *Biomacromolecules*, 2015, **16**, 1210–1217.
- 37 K. M. Schultz and K. S. Anseth, *Soft Matter*, 2013, 9, 1570–1579.
- 38 T. H. Larsen and E. M. Furst, *Phys. Rev. Lett.*, 2008, **100**, 146001.

- 39 A. J. Olsen, P. Katyal, J. S. Haghpanah, M. B. Kubilius, R. Li, N. L. Schnabel, S. C. O'Neill, Y. Wang, M. Dai, N. Singh, R. S. Tu and J. K. Montelare, *Biomacromolecules*, 2018, **19**, 1552–1561.
- 40 N. J. Greenfield, Nat. Protoc., 2006, 1, 2876-2890.
- 41 E. K. Roberts, K. M. Wong, E. J. Lee, M. M. Le, D. M. Patel and A. K. Paravastu, *Soft Matter*, 2018, **14**, 8986–8996.
- 42 S. Y. Lau, A. K. Taneja and R. S. Hodges, *J. Biol. Chem.*, 1984, 259, 13253–13261.
- 43 S. C. Kwok and R. S. Hodges, *J. Biol. Chem.*, 2004, 279, 21576–21588.
- 44 N. E. Shepherd, H. N. Hoang, G. Abbenante and D. P. Fairlie, J. Am. Chem. Soc., 2009, 131, 15877–15886.